RSC Advances

RSC Advances

www.rsc.org/advances

ROYAL SOCIETY OF CHEMISTRY

www.rsc.org/advances

Journal Name

ARTICLE

Tunable *p*-type doping of Si nanostructures for near infrared light photodetector application

Feng-Xia Liang,[a] Deng-Yue Zhang, Yi-feng Zou,[b] Han Hu, Teng-Fei Zhang,[b] Yu-Cheng Wu,[a, *] Lin-Bao Luo[b,*]

In this study, we present a simple oxide assisted *p*-type doping of Si nanostructures by evaporating a mixed powder composed of SiB_6 and SiO. It was found that Si nanoribbons (Si NRs) which can be obtained at high SiB_6 content, will give way to Si nanowires (Si NWs) when the content of SiB_6 in the mixed powder was reduced. According to our transport measurement of field effect transistors (FETs) assembled on individual Si nanostructures, the as-prepared Si nanostructures with different boron doping levels all exhibit typical *p*-type conduction characteristics. Additionally, the electrical conductivity of the Si nanostructures can be tuned over 7 orders of magnitude from 8.98×10^2 Scm^{-1} for the highly doped sample to 3.36×10^{-5} Scm^{-1} for lightly doped sample. Based on monolayer graphene and the as-prepared Si nanostructures, we also assembled a nano-photodetector which exhibits ultra-sensitivity to 850 nm near infrared light (NIR) illumination with ultra-sensitivity and nanosecond response speed (τ_{rise}/τ_{fall}: 181/233 ns). The generality of the above results suggest that the Si nanostructures are promising building blocks for future electronic and optoelectronic devices application.

Introduction

Silicon (Si) with an indirect narrow band-gap (~1.12 eV), has been central to numerous technological innovations for decades and remains to be the irreplaceable materials for semiconductor industry.[1, 2] In comparison with their thin film and bulk counterparts, one dimensional (1-D) silicon nanostructures with large surface-to-volume ratio including nanoribbons (NR),[3] nanowires (NWs),[4] and nanotubes (NTs) have exhibited various unique properties in terms of light harvesting and carrier transport.[5, 6] By this token, Si nanostructures have been lately widely used as building blocks for constructing various electronic and optoelectronic devices, such as field effect transistors (FETs),[7, 8] near infrared light (NIR) photodetectors,[9, 10] solar cells,[11, 12, 13] lithium ion batteries,[14, 15] thermoelectric devices,[16, 17] chemical or biological sensors,[18, 19] and so on.

Needless to say, the fabrication of 1-D Si nanostructures with controlled diameter, length and electronic properties are essential to the above nano-devices application. Thus far, significant efforts have been devoted to the development of facile and controlled methods for SiNW fabrication in recent years. In principle, there are two basic methodologies for Si nanostructures, i.e., the top-down (metal-catalysed chemical etching,[20] and reactive ion etching,[21] etc.) and

bottom-up approaches (oxide-assisted growth (OAG),[22] vapour-liquid-solid (VLS) growth,[23] and solid-liquid-solid (SLS).[24]). In order to tune the electrical properties of Si nanostructures, people normally employed conventional doping method, namely, intentionally incorporating impurity atoms into the host lattice of silicon crystal to control the density of the free charge carriers available in the semiconductor nanostructures, which determines the operation of the Si based nano-devices mentioned above. Take *p*-type doping for example, Cui *et al* initiated the first *p*-type silicon NWs by developing a laser-assisted catalytic growth method.[25] During growth process, boron atoms were incorporated into the Si nanostructures by using diborane (B_2H_6) in the reactant flow. According to their electrical analysis, the boron doped Si NWs had good crystal structure, with tunable electrical property. What is more, Lew found that trimethylboron (TMB) can also be used as efficient *p*-type dopant source.[26] It was found that the as-fabricated SiNWs were predominantly single crystal, with controlled boron concentrations. In spite of these efforts, it is undeniable that these gaseous dopants either in the form of B_2H_6, and $B(CH_3)_3$ are extremely toxic and flammable, which is environmentally unfriendly. As a result, their further application was greatly restricted. Herein, we present a new synthetic approach to the

synthesis of *p*-type silicon nanostructures by using SiB_6 powder as doping source. Electrical analysis revealed that the conductivity can be tuned over a large order of magnitude by adjusting the SiB_6 content in the mixed precursor. What is more, it was observed that the Schottky junction composed of monolayer graphene/individual Si nanostructures exhibited ultra-sensitivity to NIR irradiation with excellent spectral response, and fast response speed (τ_{rise}/τ_{fall}: 181/233 ns). The generality of this study suggests that the present Si nanostructures with controlled electrical property will have potential application for future electronic and optoelectronic devices.

Experimental

### Fabrication of Si nanostructures and their microstructures analysis

The preparation of the Si nanostructures was performed on a horizontal tube furnace. In brief, a mixed powder composed of SiB_6 (Analytical grade, Sigma-Aldrich Co.) and SiO (Analytical grade, Aladdin Co.) was placed at the center of the alumina tube, silicon substrates were then placed at the downstream position of the source material. Prior to heating, the system was evacuated to a base pressure of 10^{-4} Torr, and back filled with an Ar and H_2 (5%) gas mixture at a constant flow rate of 30 Sccm. Afterwards, the source was heated up to 1050 ^{o}C at a rate of 20 ^{o}C/min and then was maintained at this temperature for ~2 hours. The crystallinity, morphology and structure of the as-prepared Si nanostructures were characterized using X-ray diffractor (XRD, Siemens D-500 using Cu Kα radiation), field emission scanning electron microscopy (FESEM, Philips XL 30 FEG), transmission electron microscopy (TEM, Philips CM 20, operated at 200 kV), and high-resolution transmission electron microscopy (HRTEM, Philips CM 200 FEG, operated at 200 kV). The chemical composition of the product was analyzed by X-ray photoemission spectroscopy (XPS) which was performed on a VG ESCALAV 220i-XL surface analysis system equipped with a monochromatic Al Kα X-ray (1486.6 eV) source.

Devices fabrication and measurement

To fabricate back-gate nano Si-FET, p^+ Si substrates with 300 nm thick thermally oxidized SiO_2 were cut into small pieces (1.5×1.5 cm^2), and washed stepwise with absolute alcohol and distilled water under ultrasonication for 10 minutes, respectively. Then Si nanostructures in alcohol which was briefly treated with diluted HF solution, was dropped and dried on the Si substrate with desired density. Two parallel source and drain electrodes (2 nm Ti/58 nm Au) were then defined by photolithography, followed by electron-beam evaporation. Finally, the remaining photoresist was removed by acetone soaking. To fabricate Si nanostructure/monolayer graphene Schottky junction photodetector, the as-synthesized Si nanostructures were parallel dispersed on the substrate by contact print technique, followed by fabrication of single Ti/Au (2/58 nm) electrode on the Si nanostructure *via* photolithography, electron beam evaporation and lift-off process. Afterwards, monolayer graphene was transferred onto the one head. In order to form a good contact to the graphene, silver paste was finally placed onto the graphene film. A light system including a Xenon lamp (150 W) and a monochromator ($^1/_8$, Spectra-physics 74000) was used to provide the monochromatic light, which was focused and guided perpendicularly onto the nanowires by a quartz lens. Electrical and optoelectronic measurements were carried out on the semiconductor characterization system (4200-SCS, Keithley Co.) with picoampere resolution. Unless stated, these measurements are all carried out at room temperature. To determine the spectral response and time response of the Schottky devices, a home-built system composed of an oscilloscope (Tektronix, TDS2012B), and a pulsed LED with frequency as high as 1 MHz were used.

Results and discussion

The controlled boron doping of Si nanostructures was realized by a conventional thermal evaporation of SiB_6 and SiO powders in different ratios, which was carried out in a three-temperature-zone tube furnace, as shown in Figure 1(a). After synthesis, wool-like product (marked as Sample A, B, and C) can be obtained on the substrate by using a mixed powder composed of SiB_6 and SiO in an atomic ratio of 1:1, 1:2, 1:3, respectively (see Figure S1). Figure 1(b) shows the XRD patterns acquired from the three samples, according to which, all five peaks in the range of 20-80° can be readily ascribed to diamond-like cubic phase Si (JCPDF card no.27-1402),[27] and no obvious impurity peaks were observed. What is more, the diffraction signal of the Si nanostructures does not exhibit obvious peak shift or broadening in comparison with the standard Si, suggesting that the incorporation of boron atoms into the crystal lattice cannot alter the crystal quality of the NWs. Figure 1(c)-(e) display the FESEM images of sample A, B and C. respectively. It is visible that for sample with high boron doping level (Sample A), the product is largely composed of long ribbon-like nanostructures, the length and width of the NR are in the range of 10-30 μm and 150-500 nm, respectively. Interestingly, when we gradually reduce the content of SiB_6 in the mixed power, the as-collected products with the decrease of boron doping level (sample B and C), is mainly composed of long NWs. Although the three samples (Sample A, B and C) are different in morphology, their growth directions are highly identical to each other. Figure 1(f) and (g) show the representative TEM and HRTEM analysis of Sample A. From the corresponding lattice resolved image, one can conclude that the growth direction is along [100], in good consistence with the corresponding Fast Fourier Transformation (FFT). To study the precursor dependent morphology of the product, other precursors with controlled compositions were taken into consideration as well. It is found that when only SiB_6 were used as evaporant, Si NRs with obvious contaminant was observed. However, when the contents of SiB_6 were further reduced to 1:4 and 1:6, tortuous Si NWs with lengths of several micrometers will be obtained (Figure S2).
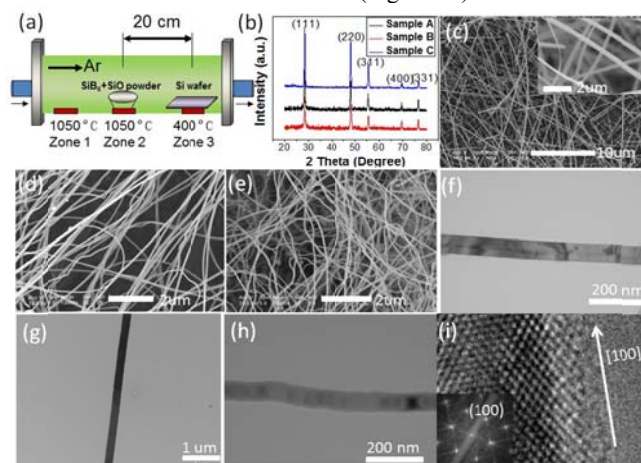

Figure 1. (a) Schematic illustration of the experimental setup for synthesis of silicon nanostructures. (b) XRD patterns of three samples. (c) SEM image of sample A which is mainly composed of Si NRs, the inset shows a SEM image at large magnification. SEM images of sample B (d) and Sample C (e). Typical TEM image of sample A (f), sample B (g), and Sample C (h). (i) HRTEM image of Si NRs, the inset shows the corresponding FFT.

Figure 2 shows a typical XPS survey spectrum of Sample A, in which five peaks at 99.5, 150.7, 189.6, 284.8 and 533.2 eV due to Si2s, Si2p, B1s, C1s, and O1s are observed. The signal C1s is attributable to surface adsorption at ambient condition. What is

more, the O1s peak can be ascribed to SiO, SiO$_2$ and oxygen due to surface adsorption. According to the B1s spectra of the three samples shown in the inset, the boron contents in the Si nanostructures (Sample A, and B) are estimated to be 1.3 and 0.037% (mole %), respectively. Moreover, the concentration of boron in the Sample C is too low to be detected. Table S1 shows the standard deviation of boron composition collected from five synthesis, from which, one can see that all samples exhibit small ($\pm$ 1.2%) standard deviation, suggesting that high reliability and reproducibility of such doping strategy. We speculate the modulation of the boron atoms concentration in the Si nanostructures was achieved by a SiB$_6$ decomposition assisted growth process: As observed in the growth of Si NW *via* OAG method, [28] at high temperature the SiO in the mixed powder will discompose to form SiO$_2$ and Si through the reaction: 2 SiO$\rightarrow$ Si (g) + SiO$_2$ (g). The Si gas will be transported to the deposition zone, where it will grow in one-dimensional way. In the meantime, the SiB$_6$ is unstable and it will decompose to form both silicon and boron atoms through the following chemical equation: SiB$_6$ (g) $\rightarrow$ Si (g) + 6B (g). The resultant boron gas is highly reactive and it can readily incorporate into the crystal lattice of silicon, giving rise to the formation of boron doped Si nanostructures. Note that, in the course of growth, the doping level is largely dependent on the SiB$_6$ content in the mixed powder, the more the SiB$_6$, the higher the doping level of silicon nanostructure will be. The doped boron distribution was determined by the EDS elemental mapping. As shown in Figure 3(c) and (d), the boron element is uniformly distributed in the Si NRs. Note that the mapping profile of boron atoms from Sample B can hardly be distinguished due to low doping level (see Figure 3 (h)).
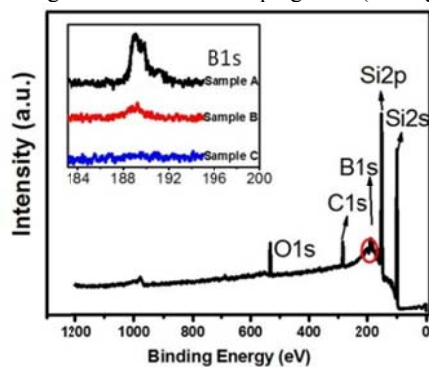
Figure 2. Survey XPS spectrum of the sample A, the inset shows the B1s spectra of Sample A, B, and C.
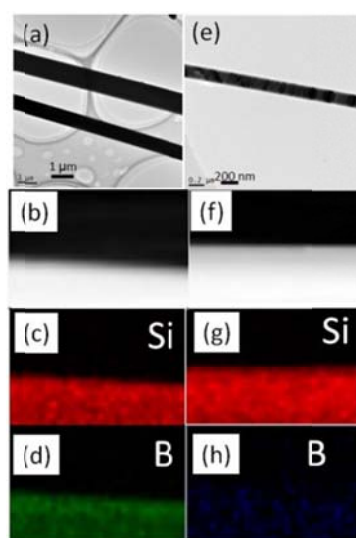

Figure 3. (a) TEM image of a boron doped Si NR from sample A. (b) Magnified TEM image of the Si NR in bright field. (c) and (d) are the corresponding EDS elemental mapping for Si and B, respectively. (e) TEM image of a boron doped Si NR from sample B. (f) Magnified TEM image of the Si NR in bright field. (g) and (h) are the corresponding EDS elemental mapping for Si and boron, respectively.

Individual nanostructure based filed-effect transistors (FETs) were fabricated to study the electrical transport properties. Figure 4(a) shows I_{ds} vs. V_{ds} curves of a FET assembled from a single highly doped Si NR (Sample A). The obvious linear curves insinuate that *Ohimic* contact was formed between the Ti/Au electrodes and the Si NR. In addition, the device exhibits a very weak *p*-type gating effect: that is, when V_g decreases (increases), the conductance increases (decreases) a lit bit (Figure 4(b)). For such a NR based FET device, the hole mobility (μ_h) of the device can be calculated by using the equation of $\mu_h = g_m L / Z C_0 V_{ds}$ [29, 30] where $g_m = dI_{ds} / dV_{gs}$ is the linear-region channel transconductance, which is actually the slope of the I_{ds}/V_{gs} shown in Figure 4 (b), Z/L is the width-to-length ratio of the channel (300 nm/3000 nm), C_0 is the capacitance of the back gate, and can be given by $C_0 = \varepsilon_r \varepsilon_0 / h$,[31] where ε_r is the dielectric constant for SiO$_2$ layer (3.9), ε_0 the vacuum permittivity (8.85×10^{-14} F•cm^{-1}), and h the thickness of the SiO$_2$ layer (300 nm). Based on the above constants and equations, the transconductance and hole mobility are estimated to be 3.0×10^{-8} S and 8.7 cm^2/Vs, respectively. In addition, the hole concentration (p) can be described by the relation of $\sigma = pq\mu_h$, where q is the elementary charge (1.6×10^{-19} C), σ is conductivity of the Si NR. The conductivity can be estimated by the formula of IL/UA, where I is the current (1.616×10^{-6} A), L is the length of the NR (3×10^{-4} m), U is the applied voltage (3 V), A is the cross-section area of the NR (300×60 nm^2). Based on these values, the conductivity and hole concentration are estimated to be 8.977×10^2 Scm^{-1} and 6.45×10^{20} cm^{-3}, respectively.

Unlike the device made from sample A, much stronger *p*-type gating effect was observed on nano-FET made from Sample B and C (cf. Figure 4(c)-(f)). The semilogarithmic plots of I_{ds} vs. V_g at a constant V_{ds}=3 V in the Figure 4(d) and (f) reveal an on/off ratios as large as 6×10^3 for Sample B, and 8×10^2 for sample C, respectively. The carrier mobility of the NW from Sample B and C cannot be estimated by the above equation, considering the fact that the building blocks has changed from NRs to NWs in morphology.[32] Assuming a cylinder on an infinite plate model for the Si NW FET (Sample B & C), the channel capacitance of the back gate can be estimated by the formula of $C = 2\pi\varepsilon_0\varepsilon_r L / \ln(4h/d)$,[33] where ε_0 and ε_r are the vacuum permittivity (8.85×10^{-14} Fcm^{-1}) and effective dielectric constant of SiO$_2$ (3.9), respectively, h the thickness of the dielectric layer, L the channel length, and d the radius of the Si NW. By fitting the linear part of the I_{ds}-V_g curve, the transconductance (g_m) is determined to be 1.37×10^{-7} S for Sample B, and 2.25×10^{-11} S for Sample C. Moreover, the hole mobility is calculated to be 15.7 cm^2/Vs (Sample B), and 2.59×10^{-3} cm^2/Vs (Sample C), respectively. By using the relation of $\sigma = pq\mu_h$ mentioned above, the hole concentrations are estimated to be 3.34×10^{17} cm^{-3} and 8.11×10^{16} cm^{-3} (Sample C) from the relation: $\mu_h = g_m L^2 / C V_{ds}$.
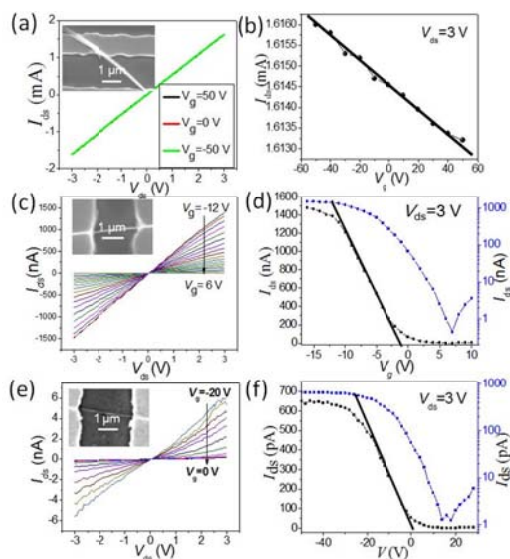
Figure 4. Electrical characteristics of Si nano-FETs. (a) I_{ds}-V_{ds} of a NR FET at different V_g. The inset shows a representative SEM image of the single NR FET. (b) Transfer characteristics of the FET at V_{ds} of 3 V. (c) I_{ds}-V_{ds} curves at different V_g of Sample B, inset in (c) is the SEM image of the NW FET. (d) The corresponding I_{ds} vs. V_g at V_{ds} of 3V. (e) I_{ds}-V_{ds} curves at different V_g of Sample C, inset in (e) is the SEM image of the NW FET. (f) The corresponding I_{ds} vs. V_g at V_{ds} of 3V.

Figure 5(a) compares the typical I-V curves of Si nanostructure from Sample A, B and C. It is revealed that the conductivity can be readily tuned over a large order of magnitude by adjusting the SiB_6 content in the precursor. To statistically evaluate the electrical conductivity of the boron doped Si nanostructures, we have in total fabricated and analyzed 30 FETs, with 10 devices from each sample (Figure 5(b)). Obviously, the conductivity of highly doped Si NR (Sample A) is very high and in the range 500-1200 Scm^{-1}. But when the doping level was gradually reduced by decreasing the SiB_6 content in the mixed precursor, the conductivity will substantially decreases to 0.5-1 Scm^{-1} for sample B, and to 0.30-1.0×10^{-5} Scm^{-1} for sample C. This result signifies that such a doping method using SiB_6 as dopant could provide an alternative doping approach for tuning the electrical conductivity of Si nanostructures. Table 1 compares the SiB_6/SiO ratio dependent electrical property of the Si nanostructures. It can be seen that the hole concentration increases continuously with increasing SiB_6 content in the mixed precursor, which suggests that the carrier concentration in the Si nanostructures can be controlled by adjusting the ratio of the precursor. However, the hole mobility increases at first from 2.57×10^{-3}, to 15.7 cm/Vs, and then decreases to 8.7 cm/Vs at high doping level. Understandably, this phenomenon is due to enhanced carrier scattering of impurity atoms in heavily doped Si nanostructures.[34]
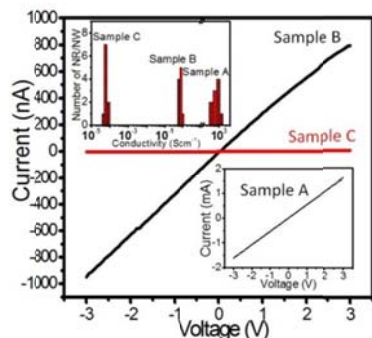

Figure 5. I-V characteristics of Si NWs (sample B & C) in the dark. The below right inset shows the I-V characteristics of Si NR (sample A) in the dark. The above left inset shows the distribution of electrical conductivity for 30 FETs from Sample A, B and C nanostructures, ten FETs for each sample.

Table 1 Summary of the key parameters of the FETs based on Si nanostructures with different doping levels.

Sample No.	SiB_6/SiO	g_m (nS)	σ (Scm^{-1})	μ_p ($cm^2V^{-1}s^{-1}$)	p (10^{17} cm^{-3})
Sample A	1:1	30	8.98×10^2	8.7	6450
Sample B	1:2	137	8.39×10^{-1}	15.7	3.34
Sample C	1:3	2.25×10^{-2}	3.36×10^{-5}	2.59×10^{-3}	0.81

Next, three kinds of silicon nanostructures/monolayer graphene heterojunction were assembled from Sample A, B, and C (cf. Figure 6(a)) in order to explore the potential for optoelectronic devices application. The monolayer graphene (MLG) was confirmed by the Raman analysis in Figure S3. The inset in Figure 7(a) shows the I-V characteristic of heterojuncton composed of the Si NR (Sample A) and MLG. Obviously, the current increases linearly with the bias voltage in the range from -5 to 5 V. This characteristic is completely different from that of Schottky junctions made from Sample B. C, in which typical rectifying behavior was observed. Such a rectifying effect can be exclusively ascribed to the graphene/Si NW considering *Ohimic* contacts were formed at both the graphene/silver paste and Ti/Au electrode/Si NW interfaces (Figure S4). Remarkably, once illuminated by NIR with wavelength of 850 nm, both Schottky junctions made from Sample B and C displayed pronounced photoresponse. As shown in Figure 7(b), the electrical current increased dramatically and stabilized at a low-resistance "on" state upon light irradiation, but decreased quickly to a high-resistance "off" state when the NIR was turned off, yielding an on/off ratio as high as 10^5. To quantitatively assess the sensitivity of the present device to NIR illumination, the specific detectivity (D^*) can be estimated by the formula of $D^* = (AR/2qI_d)^{1/2}$,[35] where A is the active area of the device, q is the elementary charge, R is the responsivity of the device, which can be described by $R = (I_p - I_d)/P_{opt}$, where I_p, I_d and P_{opt} represent the photocurrent, the dark current and the incident light power, respectively. Based on the these values, the R and D^* are estimated to be 8.7 A/W and 7.94×10^{12} $cmHz^{1/2}W^{-1}$ for sample B, and 47.3 mA/W and 1.97×10^{11} $cmHz^{1/2}W^{-1}$ for sample C at zero bias, respectively.

The device performance of the present device and other photodetector with similar structures is summarized in Table 2. Although both detectivity does not show any obvious advantage, the on/off ratio and responsivity are as high as 10^7 and 8.7 A/W, respectively, the highest values in comparison with other Si nanostructures based photodetector ever reported. Moreover, Figure 7(c) shows the photoresponse of the Gr/Sample B Schottky junction photodetector to varied illumination with different wavelengths (To make this study more reliable, the light intensity was kept identical during test). It is visible that the device exhibits good spectral selectivity, with peak sensitivity at ~960 nm.
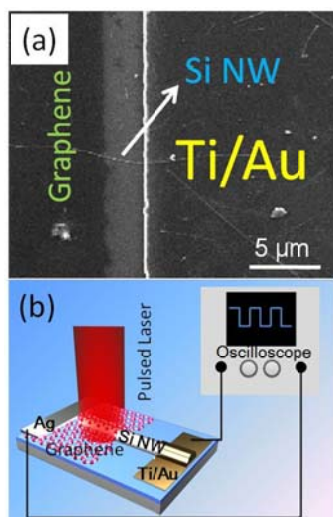
Figure 6. (a) SEM image of the monolayer graphene/Si nanostructure Schottky junction device. (b) Schematic illustration of the photoresponse measurement setup.
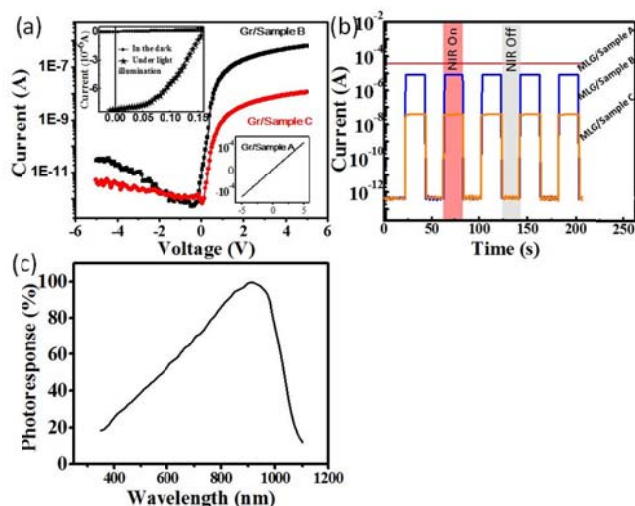
Figure 7. (a) Comparison of *I-V* curves of the graphene/NWs from both Sample B and C, the above left inset shows the *I-V* curves of Sample B in the dark and under light illumination, the below right inset shows the *I-V* curve of MLG/NW from Sample A. (b) Response of the hetero-junction device to the pulsed photo-irradiation at bias voltage of 0 V, the light wavelength was 850 nm, the powder intensity of the illumination was $\sim 9.8 \times 10^{-3}$ W/cm^2. (c) Spectral response of the MLG/Sample B NW Schottky junction device.

In addition to the high sensitivity and good spectral selectivity, the present device enjoys a slow relative balance $((I_{max} - I_{min})/I_{max})$ decay when irradiated by pulsed illumination with frequency in the range from 1 to 1 M Hz. In this study, the pulsed optical signal was generated by a light emitting diode driven by a signal generator with frequency as high as 20 M Hz. Figure 8(a) plots the relative balance as a function of switching frequency, from which one can see that the relative balance is less than 1% when the switching frequency reaches 1×10^4 Hz. Notably, even the frequency was increased to 1 M Hz, the relative balance decreases by less than 10%. This value, to the best of our knowledge is the highest ever reported, which suggests great potential for monitoring optical signal with ultra-high switching frequency.[39] It should be noted that, our Si NW/MLG Schottky junction can work properly after long-term storage at

ambient condition. As shown in Figure 8(b), the NIR photodetector can almost retain the same photocurrent after one month storage. In general, the response speed of a photodetector is often evaluated by the rise time of its response to a pulsed signal. From the magnified photoresponse curve in Figure 8(c), the rise time (τ_{rise}) and fall time (τ_{fall}) can be estimated to be 181 and 233 ns, respectively, which are far faster than other Si nanostructures based NIR photodetectors (Table 2). Two factors are considered important to this ultra-fast response speed. (1) The specific geometry of the device. In this study, the three-dimensional core-shell configuration is capable of quickly separating and collecting of the carrier by increasing the SiNW/MLG interfacial area and allowing for the diffusion of photo-generated carriers toward the depletion layer within a small distance. (2) The high-quality of the hetero-junction. Due to the formation of good Schottky junction, a built-in electric field was formed. As a result, the photo-generated carriers will be effectively and rapidly separated. This fast response speed, along with the excellent device stability renders the current device promising candidate for future nano-optoelectronc devices application.
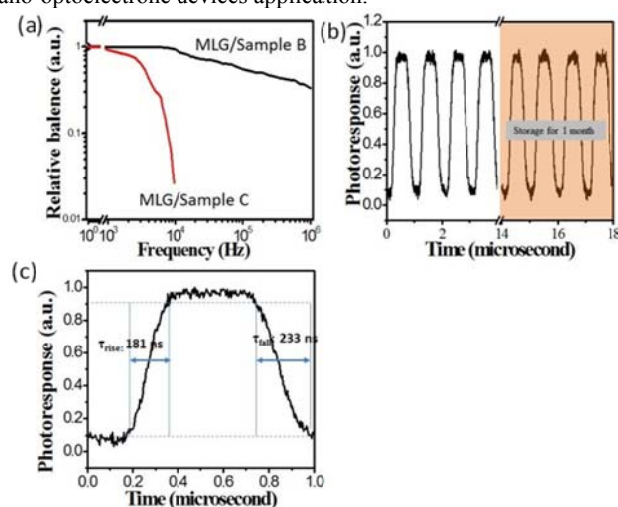
Figure 8. (a) Relative balance of both MLG/Sample B, and MLG/Sample C photodetector. (b) Photoresponse of the MLG/Sample B to pulsed near infrared light with frequency of 1 MHz. (c) A single normalized cycle of the MLG/Sample B Schottky junction photodetector for estimating both rise time and fall time.

Table 2. Comparison of the device performance of the current Si nanostructures/MLG Schottky junction with other Si bulk or nanostructures based NIRPDs.

Device Structure	Responsivity	τ_r/τ_f	I_{light}/I_{dark}	Detectivity	Ref
Individual Si NW/ MLG	8.7 A/W	181/233 ns	10^7	7.94×10^{12}	This work
Si NWs array/AuNPs@ graphene	1.5 A/W	73/96 µs	10^6	1.09×10^{14}	10
Si NWs/Carbon QDs	1.73 mA/W	20/40 µs	3×10^3	3.79×10^9	36
Si bulk /graphene NIRPD	562 mA/W	93/110 µs	1.1	3.90×10^{11}	37
n-type Si/graphene	435 mA/W	----	3×10^3	7.69×10^9	38

Conclusions

In this work, we reported on a synthetic approach to silicon nanostructures with controlled boron doping levels by a thermal evaporation of a mixed powder of SiB_6 and SiO. It is revealed that the morphology of the product is mainly determined by the content of the SiB_6 in the mixed powder. Field effect transistors (FETs) analysis shows that the as-prepared Si nanostructures all exhibit typical *p*-type conduction behaviour. The hole mobility and concentration can be readily tailored by the adjusting the content of SiB_6. It is also found that by tuning the content of the SiB_6 in the mixed powder, the electrical conductivity of the Si nanostructures can be tuned over 7 orders of magnitude from 8.98×10^2 Scm^{-1} for the highly doped sample to 3.36×10^{-5} Scm^{-1} to lightly doped sample. What is more, we observed that the Schottky junction composed of monolayer graphene/individual Si nanostructures exhibit ultra-sensitivity to 850 nm NIR irradiation with excellent spectral response, and fast response speed (τ_{rise}/τ_{fall}: 181/233 ns). We believe the present Si nanostructures with controlled electrical property will have potential application for future electronic and optoelectronic devices.

Acknowledgements

Notes and references

a School of Materials Science and Engineering and Anhui Provincial Key Laboratory of Advanced Functional Materials and Devices, Hefei University of Technology, Hefei, Anhui 230009, P. R. China Email: ycwu@hfut.edu.cn
b School of Electronic Science and Applied Physics, Hefei University of Technology, Hefei, Anhui 230009, P. R. China. Email: luolb@hfut.edu.cn
Electronic Supplementary Information (ESI) available: Digital camera pictures of the as prepared silicon nanostructures (Sample A, B, and C), digital camera pictures and SEM images of other products obtained in the ratio of 1:0, 1:4, 1:6, the synthesis of monolayer graphene, Raman spectrum of the monolayer graphene. *I-V* curves of the monolayer graphene/silver paste contact, and Ti/Au electrode/Si NW (Sample B) contact.

1. S. M. Sze, Physics of Semiconductor Devices, John Wiley & Sons: New York, 1981.
2. Y. Cui, and C. M. Lieber, Science, 2001, 291, 851-853.
3. W. Shi, H. Peng, N. Wang, C. P. Li, L. Xu, C. S. Lee, R. Kalish, and S. T. Lee, J. Am. Chem. Soc., 2001, 123, 11095-11096.
4. J. S. Jie, W. J. Zhang, K. Q. Peng, G. D. Yuan, C. S. Lee, and S. T. Lee, Adv. Funct. Mater., 2008, 18, 3251-3258.
5. E. Garnett and P. D. Yang, Nano Lett., 2010, 10, 1082-1087.
6. L. B. Luo, X. B. Yang, F. X. Liang, H. Xu, Y. Zhao, X. Xie, W. F. Zhang and S. T. Lee, J. Phys. Chem. C, 2011, 115, 18453-18458.
7. J. Goldberger, A. I. Hochbaum, R. Fan, and P. D. Yang, Nano Lett., 2006, 6, 973-977.
8. C. Celle, A. Carella, D. Mariolle, N. Chevalier, E. Eouviere, and J. P. Simonato, Nanoscale, 2010, 2, 677-680.
9. O. Hayden, R. Agarwal, and C. M. Lieber, Nat. Mater., 2006, 5, 352-356.
10. L. B. Luo, L. H. Zeng, C. Xie, Y. Q. Yu, F. X. Liang, C. Y. Wu, L. Wang, and J. G. Hu, Sci Rep., 2014, 4, 3914.
11. K. Q. Peng, and S. T. Lee, Adv. Mater., 2011, 23, 198-215.
12. L. Tsakalakos, J. Balch, J. Fronheiser, B. A. Jorevaar, O. Sulima, and J. Rand, Appl. Phys. Lett., 2007, 91, 233117.
13. M. D. Kelzenberg, D. B. Turner-Evans, B. M. Kayers, M. A. Filler, M. C. Putnam, N. S. Lewis, and H. A. Atwater, Nano Lett., 2008, 8, 710-714.
14. C. K. Chan, H. L. Peng, G. Liu, K. Mcllwrath, X. F. Zhang, R. A. Huggins, and Y. Cui, Nat. Nanotechnolol., 2008, 3, 31-35.
15. A. Magasinski, P. Dixon, B. Hertzberg, A. Kvit, J. Ayala, and G. Yushin, Nat. Mater., 2010, 9, 353-358.
16. A. I. Boukai, Y. Bunimovich, J. Tahir-Kheli, J. K. Yu, W. A. Goddard, and J. R. Heath, Nature, 2008, 451, 168-171.
17. A. Yusufu, K. Kurosaki, Y. Miyazaki, M. Ishimaru, A. Kosuga, Y. Ohishi, H. Muta, and S. Yamanaka, Nanoscale, 2014, 22, 13921-13927.
18. Y. Cui, Q. Q. Wei, H. K. Park, and C. M. Lieber, Science, 2001, 293, 1289-1292.
19. L. B. Luo, J. S. Jie, W. F. Zhang, Z. B. He, J. X. Wang, G. D. Yuan, W. F. Zhang, L. C. M. Wu, and S. T. Lee, Appl. Phys. Lett., 2009, 94, 193101.
20. C. Xie, L. B. Luo, L. H. Zeng, L. Zhu, J. J. Chen, B. Nie, J. G. Hu, Q. Li, C. Y. Wu, L. Wang and J. S. Jie, CrystEngComm, 2012, 14, 7222-7228.
21. L. A. Woldering, R. W. Tjerkstra, H. V. Jansen, I. D. Setija, and W. L. Wos, Nanotechnology, 2008, 19, 145304.
22. R. Q. Zhang, Y. Lifshitz, and S. T. Lee, Adv. Mater., 2003, 15, 635-640.
23. C. Xie, J. S. Jie, B. Nie, T. X. Yan, Q. Li, P. Lv, F. Z. Li, M. Z. Wang, C. Y. Wu, L. Wang, and L. B. Luo, Appl. Phys. Lett., 2012, 100, 193103.
24. H. F. Yan, Y. J. Xing, Q. L. Hang, D. P. Yu, Y. P. Wang, J. Xu, Z. H. Xie, and S. Q. Feng, Chem. Phys. Lett., 2000, 323, 224-227.
25. Y. Cui, X. F. Cui, J. T. Hu, and C. M. Lieber, J. Phys. Chem. B, 2000, 104, 5213-5216.
26. K. K. Lew, L. Pan, T. Bogart, S. M. Dilts, E. C. Dickey, J. M. Redwing, Y. F. Wang, M. Cabassi, T. S. Mayer, and S. W. Movak, Appl. Phys. Lett., 2004, 85, 3101-3103.
27. Z. H. Chen, J. S. Jie, L. B. Luo, H. Wang, C. S. Lee, and S. T. Lee, Nanotechnology, 2007, 18, 345502.
28. N. Wang, Y. H. Tang, Y. F. Zhang, C. S. Lee, I. Bello, and S. T. Lee, Chem. Phys. Lett., 1999, 299, 237-242.
29. J. S. Jie, W. J. Zhang, Y. Jiang, and S. T. Lee, Appl. Phys. Lett., 2006, 89, 223117.
30. L. K. Li, Y. J. Yu, G. J. Ye, Q. Q. Ge, X. D. Ou, H. Wu, D. L. Feng, X. H. Chen and Y. B. Zhang, Nat. Nanotech., 2014, 9, 372.
31. M. S. Arnold, P Avouris, Z. W. Pan and Z. L. Wang, J. Phys. Chem. B, 2003, 107, 659.
32. H. B. Huo, L. Dai, C. Liu, L. P. You, W. Q. Yang, R. M. Ma, G. Z. Ran and G. G. Qin, Nanotechnology, 2006, 17, 5912.
33. Z. Z. Hu, X. J. Zhang, C. Xie, C. Y. Wu, X. Z. Zhang, L. Bian, Y. M. Wu, L. Wang, Y. P. Zhang, and J. S. Jie, Nanoscale, 2011, 3, 4798-4803.

34. G. D. Yuan, W. J. Zhang, J. S. Jie, X. Fan, J. X. Tang, I. Shafiq, Z. Z. Ye, C. S. Lee and S. T. Lee, Adv. Mater. 2008, 20, 168-173.

35. X. Liu, L. L. Gu, Q. P. Zhang. J. Y. Wu, Y. Z. Long, and Z. Y. Fan, Nat. Commune., 2014, 5, 4007.

36. C. Xie, B. Nie, L. H. Zeng, F. X. Liang, M. Z. Wang, L. B. Luo, M. Feng, Y. Q. Yu, C. Y. Wu, Y. C. Wu and S. H. Yu, ACS Nano, 2014, 4, 4015-4022.

37. P. Lv, X. J. Zhang, X. W. Zhang, W. Deng and J. S. Jie, IEEE Elect. Dev. Lett., 2013, 34, 1337-1339.

38. X. H. An, F. Z. Liu, Y. J. Jung and S. Kar, Nano Lett., 2013, 13, 909-916.

39. Y. Jiang, W. J. Zhang, J. S. Jie, X. M. Meng, X. Fan, and S. T. Lee, Adv. Funct. Mater., 2007, 17, 1795-1800.